



 Cite this: *RSC Adv.*, 2019, 9, 30398

Widely applicable phosphomolybdic acid doped poly(9-vinylcarbazole) hole transport layer for perovskite light-emitting devices

 Yanting Wu, Zewu Xiao, Lihong He, Xiaoli Yang, Yajun Lian, Guoqing Li and Xiaohui Yang *

In this paper, a cross-linked poly(9-vinylcarbazole) (PVK):phosphomolybdic acid (PMA) layer is used as the hole transport layer in perovskite light-emitting devices, and the morphology, crystal structure, and photophysical properties of perovskite films on the PVK:PMA layer are studied. The addition of PMA into the PVK layer improves the perovskite morphology integrity and promotes hole transport. As a result, perovskite light-emitting devices using a PVK:PMA hole transport layer exhibit an improved maximum luminous efficiency of 22.1 cd A⁻¹ and power efficiency of 18.2 lm W⁻¹ when compared with those of the counterparts with a PVK hole transport layer. Efficient perovskite light-emitting devices can be accessed by using various antisolvents due to the good solvent resistance of PVK:PMA networks. Moreover, the luminous efficiencies of perovskite light-emitting devices with a PVK:PMA hole transport layer are almost invariant irrespective of the presence of a hole injection layer, illustrating wide applicability of the PVK:PMA hole transport layer in perovskite light-emitting devices.

 Received 24th July 2019
Accepted 13th September 2019

DOI: 10.1039/c9ra05734j

rsc.li/rsc-advances

Introduction

Organic–inorganic hybrid lead halide perovskites are promising for light-emitting devices due to their merits such as solution processability, band gap tunability, high luminescence efficiency, and narrow emission linewidth.^{1–7} Since the pioneering work on perovskite light-emitting devices by Tan *et al.*,¹ the performance of perovskite light-emitting devices has advanced rapidly through the effort to manipulate the composition, control the morphology, and optimize the device structure.^{2–7} To date, the best external quantum efficiencies (EQEs) of perovskite light-emitting devices have exceeded 20%, rivalling those of organic and quantum dot light-emitting devices.^{8,9}

Poly(3,4-ethylenedioxythiophene):poly(styrenesulfonate) (PEDOT:PSS) is widely used as the hole injection/transport layer in perovskite light-emitting devices due to its relatively high work function of 4.9–5.2 eV and capability to smooth the surface of the indium tin oxide (ITO) anode.^{10,11} However, PEDOT:PSS, being strongly acidic and hygroscopic, interacts with the ITO electrode and perovskite layers, which adversely affects the performance and stability of related optoelectronic devices.^{12–15} To solve the problems of PEDOT:PSS, inorganic charge transport materials such as nickel oxide (NiO_x) have been used in perovskite light-emitting devices.^{16–19} Chih *et al.*¹⁶ developed highly efficient perovskite light-emitting devices that contained a NiO_x hole injection/transport layer, which showed

a maximum luminous efficiency of 15.9 cd A⁻¹. We recently propose that addition of a UV ozone-modified organic interlayer between the cuprous thiocyanate (CuSCN) hole injection layer (HIL) and perovskite layer effectively suppresses perovskite luminescence quenching by CuSCN and simultaneously allows the subsequent layering of high quality perovskite films.¹⁹

Phosphomolybdic acid (PMA) is a kegging-type compound, which comprises a phosphorous anion and twelve molybdenum oxyanions attached by three protons.^{20–23} Quantum dot light-emitting devices containing a PMA HIL showed reduced operating voltage and improved luminous efficiency compared with the counterpart devices with a PEDOT:PSS HIL.²² PMA was shown to induce oxidative cross-linking of PVK, and resulting robust PVK:PMA networks with high resistance against the working solvents enabled preparation of solution-processed multilayer organic light-emitting devices with excellent performances.²³

Herein, we report preparation of good quality MAPbBr₃ layers on the PVK:PMA layer. The addition of PMA into PVK layer promotes hole transport in light-emitting devices. MAPbBr₃ light-emitting devices containing a PVK:PMA hole transport layer (HTL) show improved luminous efficiency and power efficiency when compared with the counterpart devices with a PVK HTL. Luminous efficiencies of MAPbBr₃ light-emitting devices containing a PVK:PMA HTL are almost invariant irrespective of the presence of a HIL, illustrating wide applicability of PVK:PMA HTL in perovskite light-emitting devices.

School of Physical Science and Technology, Southwest University, Chongqing 400715, China. E-mail: xhyang@swu.edu.cn



Results and discussion

Characterization of PVK:PMA films

We measure UV-vis absorption spectra of PVK:PMA films with different PMA concentrations annealed at 150 °C for 5 min and those of PVK:20% PMA films annealed at different temperatures for 5 min (Fig. 1a and b). All samples exhibit a similar absorption profile with an absorption edge at *ca.* 350 nm, mainly originating from PVK.²⁴ PMA shows an absorption peak at *ca.* 320 nm.²⁰ The absorbance of PVK:20% PMA layers is not changed upon CB rinsing (Fig. 1c), indicating that the layers are fully cross-linked. The work function (WF) and ionization potential (IP) of the PVK layers have been determined to be 3.58 eV and 5.98 eV with ultraviolet photoelectron spectroscopy (Fig. 1d). Addition of PMA into the PVK layer increases the WF and IP to 4.17 eV and 6.37 eV, respectively, implying that PVK layer is probably p-doped by PMA

deduced from a larger WF shift with respect to the IP shift,²⁰ which facilitates hole transport.²⁵ AFM images of the PVK and PVK:20% PMA samples annealed at 150 °C and the as-deposited PVK:20% PMA samples are shown in Fig. 1e–g, respectively. All samples show a smooth surface with the similar root-mean-square (RMS) roughness values, indicating that the addition of PMA and thermal treatment have no significant effects on the HTL morphologies. Transmission Electron Microscopy (TEM) measurements reveal that the size of PMA clusters is 25–50 nm (Fig. 1h).

Characterization of MAPbBr₃ films

Fig. 2a and b depict X-ray diffraction (XRD) patterns of MAPbBr₃ films on the ITO/CuSCN/PVK:PMA (0%, 10%, 20%), and ITO/CuSCN/PVK:20% PMA (non-baked, baked at 100 °C or 150 °C) substrates. All MAPbBr₃ films show XRD diffraction peaks at

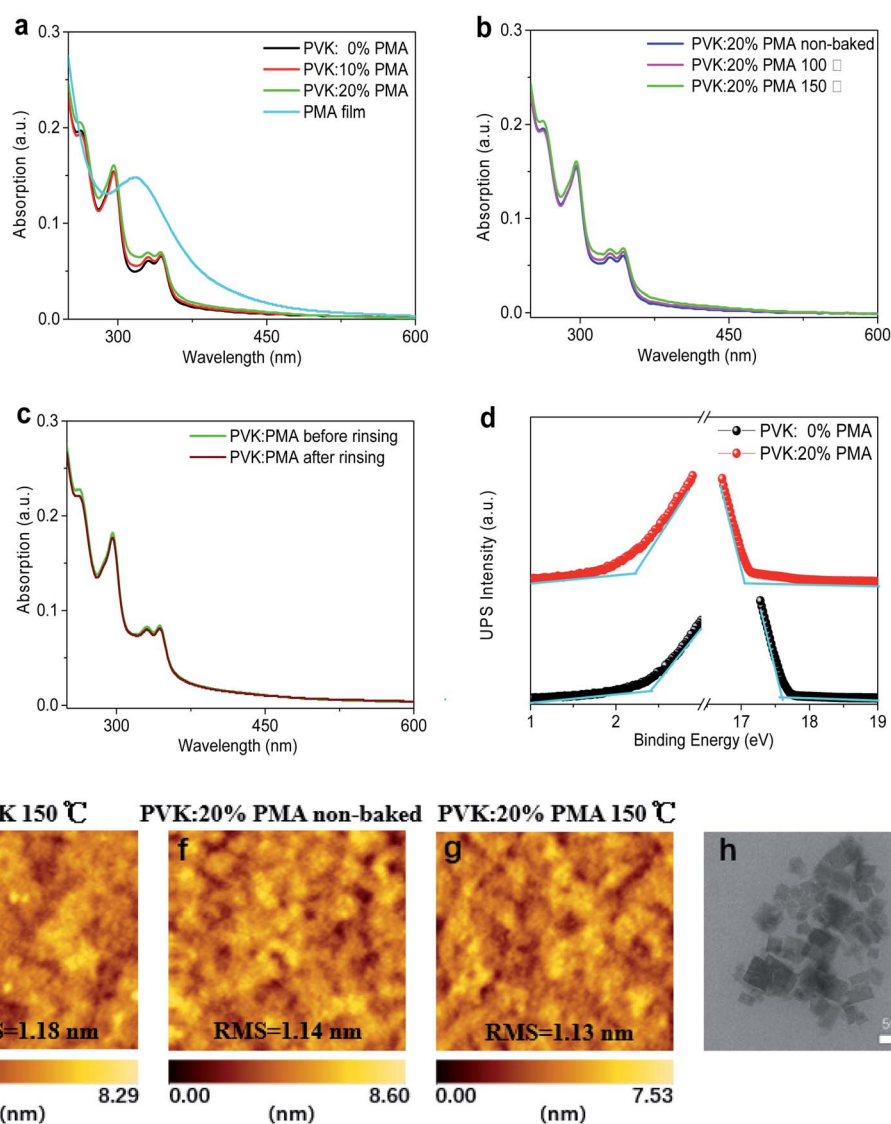


Fig. 1 (a) UV-vis absorption spectra of PMA and PVK:PMA films with different PMA concentrations annealed at 150 °C for 5 min, (b) UV-vis absorption spectra of PVK:20% PMA films annealed at different temperatures for 5 min, (c) UV-vis absorption spectra of PVK:20% PMA films and CB-rinsed PVK:20% PMA films, and (d) secondary electron cut-off and valence band regions in UPS spectra of PVK and PVK:20% PMA films. AFM images of (e) PVK:0% PMA annealed at 150 °C, PVK:20% PMA non-annealed (f) and annealed at 150 °C (g). (h) TEM image of PVK:20% PMA film.



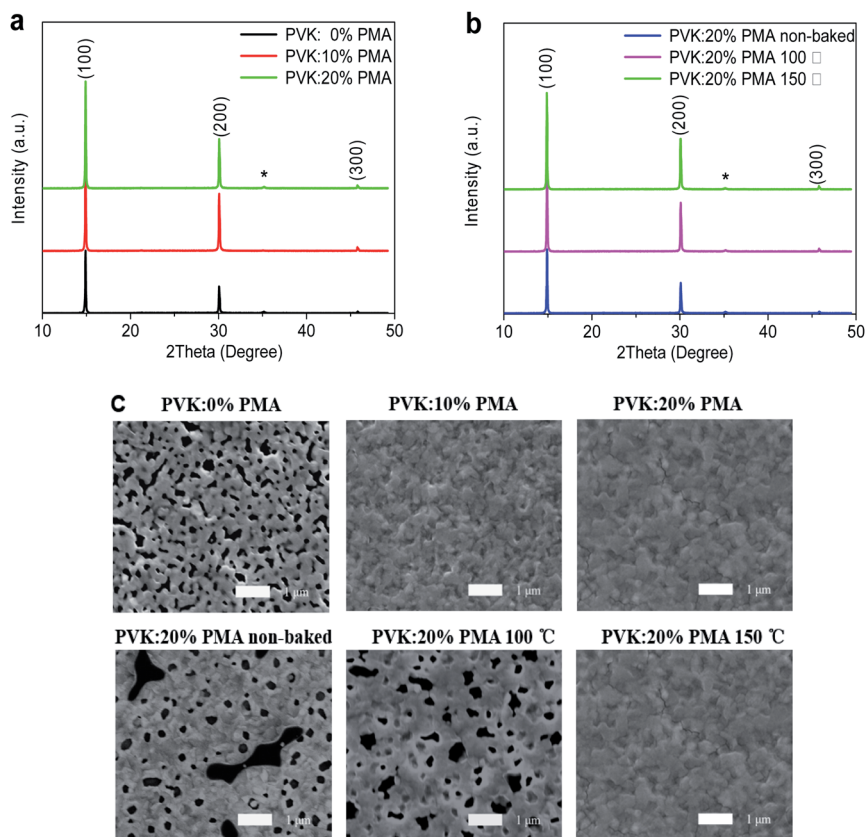


Fig. 2 (a) XRD patterns of MAPbBr₃ films on a PVK:PMA layer with different PMA concentrations, in which * represents the diffraction peak from ITO. (b) XRD patterns of MAPbBr₃ films on a PVK:20% PMA layer annealed at different temperatures. (c) Top-view SEM images of MAPbBr₃ films on a PVK:PMA layer with different PMA concentrations and those on a PVK:20% PMA layer annealed at different temperatures.

14.9°, 30.0°, and 45.8°, which are originated from the (100), (200), and (300) crystal planes of the MAPbBr₃ cubic crystal structure, respectively.²⁶ The (100) diffraction peak intensity increases upon the addition of PMA into the PVK layer and is not changed when the PMA concentration is increased from 10% to 20%, indicating that incorporation of PMA slightly increases MAPbBr₃ crystallinity. Similarly, the (100) diffraction peak intensity of the sample slightly increases following thermal treatment of PVK:20% PMA layers at 100 °C and 150 °C.

Top-view SEM images of MAPbBr₃ films on the PVK:20% PMA samples treated at different temperatures are shown in Fig. 2c. The substrate coverages of MAPbBr₃ films increase with the increasing treatment temperature. MAPbBr₃ films on the PVK:20% PMA layer treated at 150 °C appear fully continuous and have negligible holes or cracks. The underlying reason for this is not clear at the present stage. We hypothesize it may relate to small amount of water in PMA sample. Ohisa *et al.*²⁰ reported that the water content in PMA powder increased when stored in the ambient conditions. And water was reported to induce the change of MAPbBr₃ crystallinity and the formation of cracks and pin-holes.²⁷ Top-view SEM images of MAPbBr₃ films on the PVK:PMA layers with different PMA concentrations treated at 150 °C are also shown in Fig. 2c. It appears that the PMA aids to improve the MAPbBr₃ morphology integrity.

The PL maxima of all MAPbBr₃ samples occur at 529 nm, as shown in Fig. 3a and b. PL intensities of MAPbBr₃ films decrease with increasing PMA concentration (Fig. 3a), which is possibly attributed to electron transfer from MAPbBr₃ to PMA with a deep-lying WF of 6.4 eV.²⁰ Time-resolved PL decay plots of the MAPbBr₃ samples are shown in Fig. 3c. All PL decay curves can be fitted with a double exponential function, where the fast and slow components correspond to trap-mediated non-radiative recombination process and radiative electron-hole bimolecular recombination process, respectively.²⁸ The fitting parameters are provided in Table 1. The average lifetime of MAPbBr₃ films on the PVK layer (21.38 ns) is longer than those of MAPbBr₃ films on the PVK:10% PMA layer (11.68 ns) and PVK:20% PMA layer (9.55 ns), which is in line with the steady-state PL measurement results.

In addition, as the annealing temperature for PVK:20% PMA layers increases, PL intensity of the overlying MAPbBr₃ layer is elevated (Fig. 3b), which may be associated with improved morphology integrity and reduced defect density in MAPbBr₃ films.

Light-emitting devices

Light-emitting devices with the structure of ITO/CuSCN (15 nm)/PVK:PMA (30 nm)/MAPbBr₃ (75 nm)/TmPyPB (60 nm)/CsF (1 nm)/Al (100 nm) are prepared to investigate the effects of PVK:PMA HTL incorporation on MAPbBr₃ electroluminescent (EL) properties.



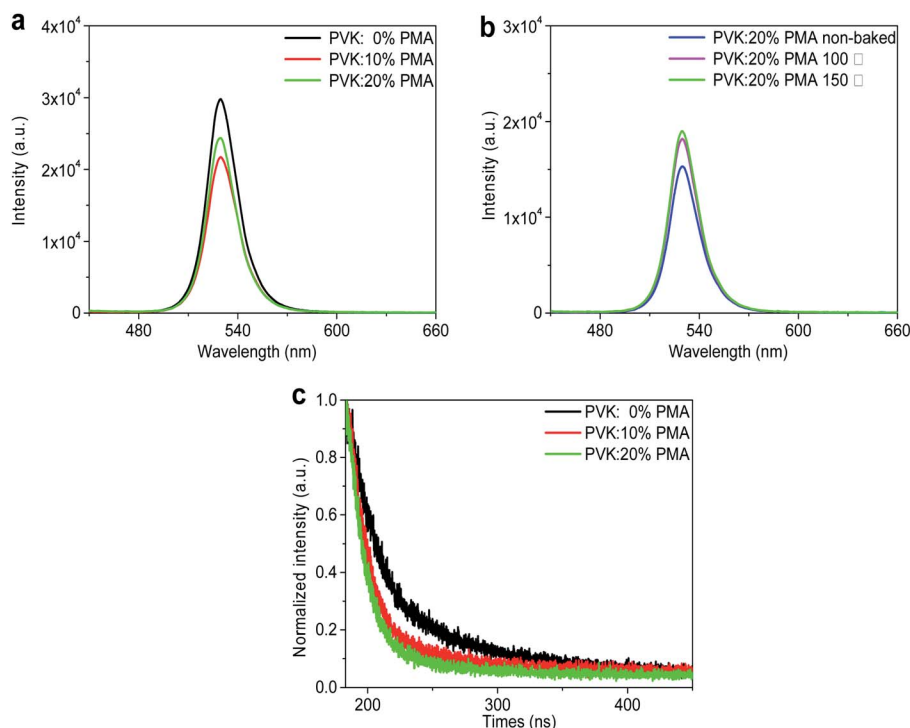


Fig. 3 (a) PL spectra of MAPbBr₃ films on the PVK:PMA layer with different PMA concentrations, (b) PL spectra of MAPbBr₃ films on the PVK:20% PMA layer annealed at different temperatures. (c) Time-resolved PL decay curves of MAPbBr₃ films on the PVK:PMA layer with different PMA concentrations.

Schematic diagrams of the devices and their energy levels are shown in Fig. 4a and b. The inset shows a cross-sectional SEM image of a MAPbBr₃ layer on the PVK:20% PMA layer treated at 150 °C. A compact MAPbBr₃ layer with the thickness of *ca.* 70–100 nm forms a good contact with the PVK:PMA layer. Except the energy levels of PVK:PMA layers (Fig. 1d), the energy levels of other materials and

work function of the electrodes are obtained from the literature.^{3,26,29} The *J–L–V* and luminous efficiency–current density characteristics of the devices that contain a PVK:PMA HTL with different PMA concentrations are shown in Fig. 5a and b, respectively. Under certain voltage, current density of the devices increases with increasing PMA concentration, indicating that the addition of PMA into PVK layer promotes hole transport. Hole-dominated devices containing a PVK:20% PMA layer show larger current compared with that of the counterpart devices containing a PVK layer, confirming enhanced hole transport in the devices containing a PVK:PMA HTL (Fig. 5c). Meanwhile, the maximum luminous efficiencies of the devices increase with increasing PMA concentration, which is mainly associated with improved MAPbBr₃ morphology integrity. Among the devices, the PVK:20% PMA device shows the highest maximum luminous efficiency of 22.1 cd A^{−1} and power efficiency of 18.2 lm W^{−1}, respectively.

Table 1 Fitting parameters for the time-resolved PL decay curves of MAPbBr₃ films on the PVK:PMA layer with different PMA concentrations

	τ_1 (ns)	A_1 (%)	τ_2 (ns)	A_2 (%)	τ_{ave} (ns)
PVK:0% PMA	10.44	72	49.81	28	21.38
PVK:10% PMA	7.77	91	49.04	9	11.68
PVK:20% PMA	6.89	92	41.25	8	9.55

Table 2 Summarization of the metrics of light-emitting devices using a PVK:PMA HTL with different PMA concentrations or with a PVK:20% PMA HTL treated at different annealing temperatures

HTLs	LE _{max} (cd A ^{−1})	PE _{max} (lm W ^{−1})	Luminance @ 6 V (cd m ^{−2})
PVK:0% PMA	16.2	12.1	3324
PVK:10% PMA	19.0	14.8	12 330
PVK:20% PMA	22.1	18.2	11 600
PVK:20% PMA non-baked	0.7	0.4	1178
PVK:20% PMA 100 °C	2.8	1.7	4492
PVK:20% PMA 150 °C	22.1	18.2	11 600



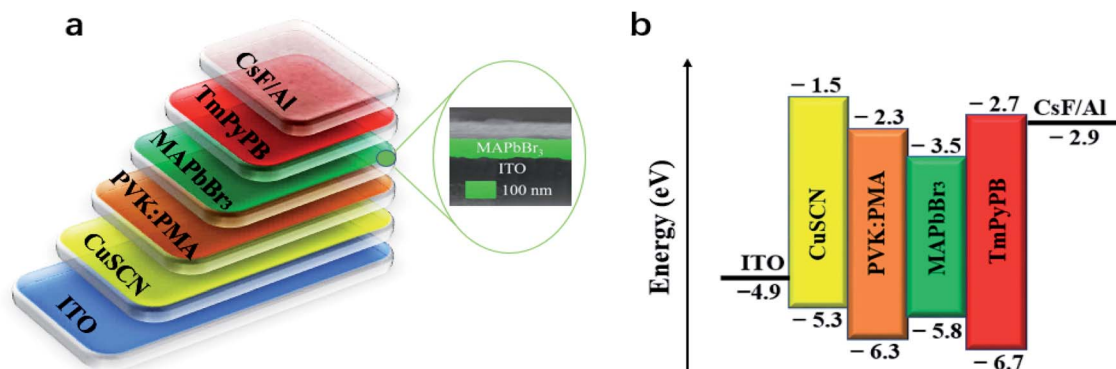


Fig. 4 (a) Schematic diagrams of the devices and (b) their energy levels. The inset shows a cross-sectional SEM image of a MAPbBr₃ layer on the CuSCN/PVK:20% PMA bilayer pre-coated ITO substrate.

We fix the PMA concentration to 20% and investigate how the thermal treatment temperature for PVK:PMA layers affects the performance of perovskite light-emitting devices. The J - L - V and luminous efficiency-current density characteristics of the devices

are shown in Fig. 5d and e. Compared with the devices containing a PVK:20% PMA layer treated at 150 °C, the devices with an as-deposited PVK:20% PMA layer or with a PVK:20% PMA layer treated at 100 °C exhibit inferior maximum luminous efficiencies of

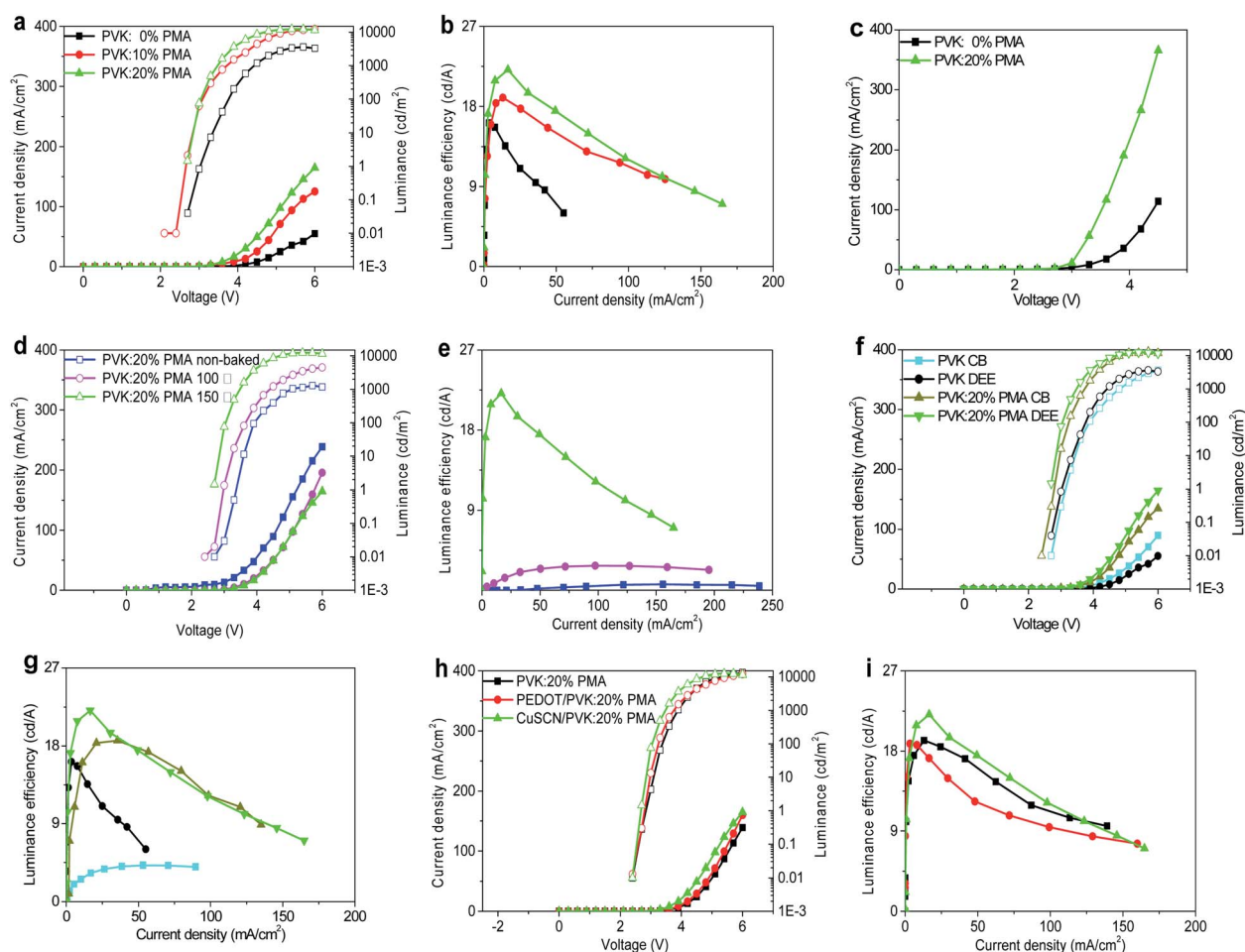


Fig. 5 (a) J - L - V and (b) luminous efficiency-current density characteristics of light-emitting devices using a PVK:PMA HTL with different PMA concentrations. (c) J - V characteristics of the hole-dominated devices with the structure of ITO/CuSCN/PVK or PVK:20% PMA/MAPbBr₃/mCP/Ag. (d) J - L - V and (e) luminous efficiency-current density properties of light-emitting devices using a PVK:20% PMA HTL annealed at different temperatures. (f) J - L - V and (g) luminous efficiency-current density plots of light-emitting devices using a PVK:20% PMA or PVK HTL processed with a CB or DEE antisolvent. (h) J - L - V and (i) luminous efficiency-current density curves of light-emitting devices with different HTLs.



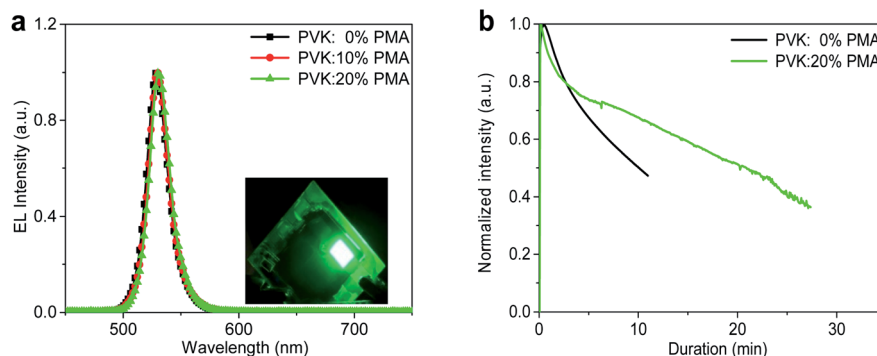


Fig. 6 (a) EL spectra of light-emitting devices using a PVK:PMA HTL with different PMA concentrations. The inset shows a photo of a lit device with a PVK:20% PMA HTL. (b) Operational stability measurements of light-emitting devices with a PVK:20% PMA or a PVK HTL under 3 mA cm^{-2} .

0.7 cd A^{-1} and 2.8 cd A^{-1} , respectively, which may relate to the combinational effects of poor MAPbBr₃ morphology integrity and high defect density in MAPbBr₃ layers, as revealed by the SEM and steady-state PL measurements (Table 2).

Due to the cross-linking nature of PVK:PMA layers, properties of light-emitting devices processed with a CB or DEE antisolvent are similar, as shown in Fig. 5f and g. By contrast, DEE-processed light-emitting devices with a PVK HTL show much higher luminous efficiencies compared with the counterpart devices processed with CB due to damaging PVK layer by CB. The results indicate use of a PVK:PMA HTL allows the wide range antisolvent selection to optimize the properties of MAPbBr₃ layers without disrupting device structure.

To further illustrate wide applicability of a PVK:PMA HTL, we prepare light-emitting devices devoid of HIL, with a PEDOT:PSS or CuSCN HIL, *i.e.* with the structure of ITO/HIL/PVK:20% PMA (30 nm)/MAPbBr₃ (75 nm)/TmPyPB (60 nm)/CsF (1 nm)/Al (100 nm) and measure the *J-L-V* and luminous efficiency-current density characteristics of light-emitting devices, which are shown in Fig. 5h and i. The devices with a PVK:PMA HTL show similar luminous efficiencies irrespective of the presence of a HIL, which may relate to that PVK is p-doped by PMA,²⁵ demonstrating wide applicability of PVK:PMA layer in perovskite light-emitting devices. Note that the devices with a CuSCN or PEDOT:PSS HIL show slightly larger current compared with the devices devoid of a HIL.

The devices containing a PVK:PMA HIL with different PMA concentrations all exhibit the characteristic MAPbBr₃ emission with a maximum at 529 nm and a full width at half maximum (FWHM) value of *ca.* 20 nm (Fig. 6a), rendering a pure green emission with Commission Internationale de l'Eclairage (CIE) chromaticity coordinates of (0.195, 0.751). Light emission from the device with a PVK:20% PMA HIL is uniform (Fig. 6a, inset). The operational stability measurements of the devices containing a PVK or PVK:20% PMA HTL are shown in Fig. 6b. The operational lifetime (T_{50}) of the devices containing a PVK HTL, when driven at 3 mA cm^{-2} , is approximately 11 min. Under the same driving conditions, the devices with a PVK:20% PMA HTL exhibit a lifetime of 22 min. Improved MAPbBr₃ morphology integrity on a PVK:20% PMA layer contributes to enhanced operational stability of light-emitting devices by reducing the shunt paths. Meanwhile, the addition of

PMA decreases operating voltage of light-emitting devices, and as a result may reduce the effect of Joule heating on the longevity of light-emitting devices.³⁰

Conclusion

Addition of PMA into PVK layer aids to form good quality MAPbBr₃ layer and facilitates hole transport, nevertheless, slightly quenches MAPbBr₃ luminescence. Perovskite light-emitting devices that contain a PVK:PMA HTL exhibit a maximum luminous efficiency of 22.1 cd A^{-1} and power efficiency of 18.2 lm W^{-1} , respectively, which are superior to those of the counterpart devices containing a PVK HTL. Use of a PVK:PMA HTL allows wide range antisolvent selection due to its cross-linking nature. In addition, the devices with a PVK:PMA HTL show similar luminous efficiencies irrespective of the presence of a HIL, demonstrating wide applicability of PVK:PMA layer in perovskite light-emitting devices.

Experiment section

Materials

Methylammonium bromide (MABr), lead(II) bromide (PbBr₂), 1,3,5-tri(*m*-pyrid-3-yl-phenyl)benzene (TmPyPB), and 1,3-bis(*N*-carbazolyl)benzene (mCP) were purchased from Xi'an Polymer Technology (China). Poly(3,4-ethylenedioxythiophene):poly(styrenesulfonate) (PEDOT:PSS) (AI 4083) was obtained from Heraeus Corp. (Germany). CuSCN, dimethylformamide (DMF), chlorobenzene (CB), diethyl ether (DEE), and PVK were bought from Sigma-Aldrich (China). Diethyl sulfide (DES) was obtained from Shanghai Aladdin Industrial Corporation (China). Acetonitrile was purchased from Tianjin Kermel Chemical Testing Corp. (China). PMA was bought from Tokyo Chemical Industry Corp. All materials were used as received.

Device fabrication

CuSCN powder was dissolved in DES with a concentration of 20 mg ml^{-1} at 60°C for 1 h. PVK and mCP were dissolved in CB with respective concentrations of 6 and 8 mg ml^{-1} . PMA was dissolved in acetonitrile with a concentration of 5 mg ml^{-1} . MABr (63 mg, 0.53 mmol) and PbBr₂ (137 mg, 0.37 mmol) were



dissolved into 1 ml DMF. ITO substrates were sequentially cleaned with deionized water and organic solvents and afterward treated with UV ozone for 30 min immediately prior to device preparation. For preparation of a CuSCN HIL, the CuSCN solution was spin-coated onto the ITO substrates at 5000 rpm for 60 s. The CuSCN layers were heated at 60 °C for 3 min. For preparation of a PEDOT:PSS HIL, the PEDOT:PSS water dispersion was spin-coated on the ITO substrates, which were thermally treated at 170 °C for 10 min to remove residual water. PVK and PVK:PMA HTLs were prepared by spin-coating the solutions at 3000 rpm on the ITO substrates, PEDOT:PSS, or CuSCN layers. The PVK:PMA layers were subsequently treated at different temperatures for 5 min. The MAPbBr₃ precursor solution was spin-coated at 3000 rpm. During the film formation process, 400 µl DEE or CB was dropped onto the spinning substrate to accelerate crystallization. The thickness of the MAPbBr₃ layer was *ca.* 75 nm as determined from the cross-sectional SEM measurements. Light-emitting devices were completed by sequentially depositing TmPyPB (60 nm), CsF (1 nm), and Al (100 nm) under a vacuum of 10^{−4} Pa onto the MAPbBr₃ layers. Hole-dominated devices were prepared by the successive deposition of mCP (15 nm) and Ag (100 nm) onto the MAPbBr₃ layers. All preparation processes were conducted inside a glovebox with water and oxygen concentrations of 1 ppm except for deposition of PEDOT:PSS layers.

Device characterization

The device's current density–luminance–voltage (*J–L–V*) characteristics were measured using a programmed Keithley 2400 source-measure unit and a Konica-Minolta chroma meter CS-100A. Electroluminescent (EL) spectra were recorded with an Ocean Optics USB4000 UV-vis spectrometer. UV-vis absorption spectra were characterized with a Shimadzu UV-2600 spectrophotometer. Steady-state PL spectra and time-resolved PL decay curves were acquired with a Hitachi F4600 fluorophotometer using an excitation wavelength of 405 nm. X-ray diffraction (XRD) patterns were measured with a Rigaku D/Max-B X-ray diffractometer equipped with a Cu K α radiation source. Morphologies of the samples were studied using a JSM-7100 scanning electron microscope (SEM) and a Hitachi atomic force microscope (AFM). Ultraviolet photoelectron spectroscopy (UPS) measurements were performed using an ESCALAB 250Xi system. Transmission electron microscopy measurements were carried out with a FEI Talos F200 scanning/transmission electron microscope.

Conflicts of interest

There are no conflicts to declare.

Acknowledgements

Financial support by the National Natural Science Foundation of China (Grant No: 11474232).

References

- 1 Z. K. Tan, R. S. Moghaddam, M. L. Lai, P. Docampo, R. Higler, F. Deschler, M. Price, A. Sadhanala, L. M. Pazos, D. Credgington, F. Hanusch, T. Bein, H. J. Snaith and R. H. Friend, *Nat. Nanotechnol.*, 2014, **9**, 687–692.
- 2 H. Cho, S. H. Jeong, M. H. Park, Y. H. Kim and T. W. Lee, *Science*, 2015, **350**, 1222–1225.
- 3 S. A. Veldhuis, P. P. Boix, N. Yantara, M. J. Li, T. C. Sum, N. Mathews and S. G. Mhaisalkar, *Adv. Mater.*, 2016, **28**, 6804–6834.
- 4 L. N. Quan, F. P. G. de Arquer, R. P. Sabatini and E. H. Sargent, *Adv. Mater.*, 2018, **30**, 1801996.
- 5 S. D. Stranks and H. J. Snaith, *Nat. Nanotechnol.*, 2015, **10**, 391–402.
- 6 N. N. Wang, L. Cheng, R. Ge, S. T. Zhang, Y. F. Miao, W. Zou, C. Yi, Y. Sun, Y. Cao, R. Yang, Y. Q. Wei, Q. Guo, Y. Ke, M. T. Yu, Y. Z. Jin, Y. Liu, Q. Q. Ding, G. C. Xing, H. Tian, C. H. Jin, F. Gao, R. H. Friend, J. P. Wang and W. Huang, *Nat. Photonics*, 2016, **10**, 699–704.
- 7 B. R. Sutherland and E. H. Sargent, *Nat. Photonics*, 2016, **10**, 295–302.
- 8 Y. Cao, N. Wang, H. Tian, J. Guo, Y. Wei, H. Chen, Y. Miao, W. Zou, K. Pan, Y. He, H. Cao, Y. Ke, M. Xu, Y. Wang, M. Yang, K. Du, Z. Fu, D. Kong, D. Dai, Y. Jin, G. Li, H. Li, Q. Peng, J. Wang and W. Huang, *Nature*, 2018, **562**, 249–253.
- 9 K. Lin, J. Xing, L. N. Quan, F. P. G. de Arquer, X. Gong, J. Lu, L. Xie, W. Zhao, D. Zhang, C. Yan, W. Li, X. Liu, Y. Lu, J. Kirman, E. H. Sargent, Q. Xiong and Z. Wei, *Nature*, 2018, **562**, 245–248.
- 10 S. Ahn, S. H. Jeong, T. H. Han and T. W. Lee, *Adv. Opt. Mater.*, 2017, **5**, 1600512.
- 11 Y. W. Zhu, Z. C. Yuan, W. Cui, Z. W. Wu, Q. J. Sun, S. D. Wang, Z. H. Kang and B. Q. Sun, *J. Mater. Chem. A*, 2014, **2**, 1436–1442.
- 12 M. Jorgensen, K. Norrman and F. C. Krebs, *Sol. Energy Mater. Sol. Cells*, 2008, **92**, 686–714.
- 13 H. Luo, X. Lin, X. Hou, L. Pan, S. Huang and X. Chen, *Nano-Micro Lett.*, 2017, **9**, 39.
- 14 G. A. D. Benatto, B. Roth, M. V. Madsen, M. Hosel, R. R. Sondergaard, M. Jorgensen and F. C. Krebs, *Adv. Energy Mater.*, 2014, **4**, 1400732.
- 15 D. W. Zhao, M. Sexton, H. Y. Park, G. Baure, J. C. Nino and F. So, *Adv. Energy Mater.*, 2015, **5**, 1401855.
- 16 Y. K. Chih, J. C. Wang, R. T. Yang, C. C. Liu, Y. C. Chang, Y. S. Fu, W. C. Lai, P. Chen, T. C. Wen, Y. C. Huang, C. S. Tsao and T. F. Guo, *Adv. Mater.*, 2016, **28**, 8687–8694.
- 17 Z. B. Wang, Z. Luo, C. Y. Zhao, Q. Guo, Y. P. Wang, F. Z. Wang, X. M. Bian, A. Alsaedi, T. Hayat and Z. A. Tan, *J. Phys. Chem. C*, 2017, **121**, 28132–28138.
- 18 L. Liu, Z. B. Wang, W. D. Sun, J. Zhang, S. Q. Hu, T. Hayat, A. Alsaedi, T. Hayat and Z. A. Tan, *Chem. Commun.*, 2018, **54**, 13283–13286.
- 19 Y. T. Wu, Z. W. Xiao, Y. J. Lian, X. F. Peng, L. L. He, X. L. Yang, Q. Wang, J. Ren, G. Q. Li and X. H. Yang, *Org. Electron.*, 2019, **75**, 105420.



- 20 S. Ohisa, S. Kagami, Y. J. Pu, T. Chiba and J. Kido, *ACS Appl. Mater. Interfaces*, 2016, **8**, 20946–20954.
- 21 M. Chrzanowski, M. Banski, P. Sitarek, J. Misiewicz and A. Podhorodecki, *RSC Adv.*, 2019, **9**, 10754–10759.
- 22 D. Dong, L. Lian, H. Wang and G. F. He, *Org. Electron.*, 2018, **62**, 320–326.
- 23 N. Aizawa, Y. J. Pu, T. Chiba, S. Kawata, H. Sasabe and J. Kido, *Adv. Mater.*, 2014, **26**, 7543–7546.
- 24 C. Zhang, H. Von Seggern, K. Pakbaz, B. Kraabel, H. W. Schmidt and A. J. Heeger, *Synth. Met.*, 1994, **62**, 35–40.
- 25 G. F. He, K. Leo, M. Hofmann, J. Birnstock, R. Pudzich and J. Salbeck, *Appl. Phys. Lett.*, 2004, **85**, 3911–3913.
- 26 X. F. Peng, X. Y. Wu, X. X. Ji, J. Ren, Q. Wang, G. Q. Li and X. H. Yang, *J. Phys. Chem. Lett.*, 2017, **8**, 4691–4697.
- 27 H. R. Wang, X. M. Li, M. J. Yuan and X. Y. Yang, *Small*, 2018, **14**, 1703410.
- 28 J. Z. Chen and N. G. Park, *Adv. Mater.*, 2018, **30**, 1803019.
- 29 Q. Xiong, H. Tian, J. Zhang, L. Han, C. Y. Lu, B. H. Shen, Y. Zhang, Y. J. Zheng, C. J. Lu, Z. B. Zeng, Z. Y. Hu, L. H. Wu and Y. J. Zhu, *Org. Electron.*, 2018, **61**, 151.
- 30 Z. G. Xiao, R. A. Kerner, L. F. Zhao, N. L. Tran, K. M. Lee, T. W. Koh, G. D. Scholes and B. P. Rand, *Nat. Photonics*, 2017, **11**, 108–115.

